Mon. Not. R. Astron. Soc. **000**, 000–000 (0000) Printed 7 March 2011 (MN LATEX style file v2.2)

Creation of cosmic structure in the complex galaxy cluster merger Abell 2744

J. Merten,[1,2⋆†] D. Coe,[3⋆] R. Dupke,[4,5,6] R. Massey,[7] A. Zitrin,[8] E. Cypriano,[9] N. Okabe,[10,11] B. Frye,[12] F. Braglia,[13] Y. Jiménez-Teja,[14] N. Benítez,[14] T. Broadhurst,[15,16] J. Rhodes,[17] M. Meneghetti,[2] L. Moustakas,[17] L. Sodre,[7] J. Krick,[18] J. N. Bregman[4] and R. A. Bernstein[19]

[1] *Institut für Theoretische Astrophysik, ZAH, Albert-Ueberle-Straße 2, 69120 Heidelberg, Germany*
[2] *INAF-Osservatorio Astronomico di Bologna, Via Ranzani 1, 40127 Bologna, Italy*
[3] *Space Telescope Science Institute, Baltimore, MD 21218, USA*
[4] *University of Michigan, Ann Arbor, MI 48109-1090, USA*
[5] *Eureka Scientific, 2452 Delmer Street 100, Oakland CA, USA*
[6] *Observatório Nacional, Rua General José Cristino 77, Rio de Janeiro, 20921-400, Brazil*
[7] *University of Edinburgh, Royal Observatory, Blackford Hill, Edinburgh EH9 3HJ, UK*
[8] *School of Physics and Astronomy, Raymond and Beverly Sackler Faculty of Exact Sciences, Tel Aviv University, Tel Aviv 69978, Israel*
(Additional affiliations after the conclusions)

7 March 2011

ABSTRACT

We present a detailed strong lensing, weak lensing and X-ray analysis of Abell 2744 ($z = 0.308$), one of the most actively merging galaxy clusters known. We dub the system *Pandora's Cluster*, because it appears to have unleashed 'dark', 'ghost', 'bullet' and 'stripped' substructures, each $\sim 10^{14} M_{\odot}$. The phenomenology is complex and will present a challenge for numerical simulations to reproduce. With new, multiband *HST* imaging, we identify 34 strongly-lensed images of 11 galaxies around the massive Southern 'core'. Combining this with weak lensing data from *HST*, *VLT* and *Subaru*, we produce the most detailed mass map of this cluster to date. We also perform an independent analysis of archival *Chandra* X-ray imaging. Our analyses support a recent claim that the Southern core and Northwestern substructure are post-merger and exhibit morphology similar to the *Bullet Cluster* viewed from an angle. From the separation between gas and mass in the Southern core, we derive a new and independent constraint on the self-interaction cross section of dark matter particles $\sigma/m \lesssim 3$ cm^2/g. In the Northwestern substructure, the gas, dark matter, and galaxy components have become separated by much larger distances. Most curiously, the 'ghost' clump (primiarly gas) *leads* the 'dark' clump (primarily dark matter) by nearly 500 kpc. We propose an enhanced 'ram-pressure slingshot' scenario which may have yielded this reversal of components with such a large separation, but needs further confirmation by follow-up observations and numerical simulations. A secondary merger involves a second 'bullet' clump in the North and an extremely 'stripped' clump to the West. The latter, yet to be discussed in the literature, appears to exhibit the largest separation between dark matter and baryons detected to date in our sky.

Key words: Dark matter — Gravitational lensing: strong — Gravitational lensing: weak — X-rays: galaxies: clusters — Galaxies: clusters: individual: Abell 2744.

1 INTRODUCTION

The standard ΛCDM cosmological model suggests a bottom-up sequence of structure formation, in which a series of merging events culminates in massive clusters of galaxies, the latest structures to form in the observable Universe (Bond et al. 1991; Lacey & Cole 1993). The number of clus-

⋆ Both authors contributed equally to this work
† E-mail: jmerten@ita.uni-heidelberg.de

ters as a function of their mass (the steep, high end of the mass function) depends sensitively upon cosmological parameters (e.g. Vikhlinin et al. 2009) and has become an important observational test of cosmology. Most measurements of cluster masses rely upon the calibration of more easily observable proxies, such as X-ray luminosity, temperature or galaxy richness. However, clusters form through multiple, dynamic accretions, so are likely to be turbulent places, and the turmoil affects those observable proxies. It is therefore vital to quantitatively understand the merging process, for example by mapping the distribution of dark matter distribution, stars and baryonic gas in systems at many different stages of merging process.

Merging clusters of galaxies have become useful laboratories in which to study the nature and interaction properties of dark matter. The best-studied example is the *Bullet Cluster* 1ES 0657-558 (Tucker et al. 1998; Markevitch et al. 2002). Combined X-ray and gravitational lensing analyses show a clear separation between the centres of X-ray emission and the peaks in surface mass density – indicating a fundamental difference between baryonic gas, which feels the pressure of the collision, and dark matter, which is nearly collisionless (Clowe et al. 2004, 2006; Bradač et al. 2006). The discovery and interpretation of the *Bullet Cluster* has inspired a lively debate about whether such a system could exist in different cosmological models (see e.g. Hayashi & White 2006). Improvements are continuing in numerical simulations (Milosavljević et al. 2007; Springel & Farrar 2007; Mastropietro & Burkert 2008; Lee & Komatsu 2010). Observations have also broadened, with discoveries of a possible line-of-sight merger CL0024+1654 (Czoske et al. 2002; Hoekstra 2007; Jee et al. 2007; Zitrin et al. 2009; Umetsu et al. 2010; Zu Hone et al. 2009b,a), and other systems including the *Baby Bullet* (MACS J0025.4-1222) (Bradač et al. 2008), the *Cosmic Train Wreck* (Abell 520) (Mahdavi et al. 2007), Abell 2146 (Russell et al. 2010), Abell 521 (Giacintucci et al. 2008) and Abell 3667 (Finoguenov et al. 2010). All these systems place potentially tight constraints on the interaction between baryons and dark matter, as well as exemplary probes for our understanding of structure formation within gravitationally bound systems.

In the archival data of 38 merging clusters, Shan et al. (2010) found the largest offset between X-ray and lensing signals to occur in the massive ($L_X = 3.1{\times}10^{45}$ erg/s in the 2-10 keV range Allen (1998)) cluster Abell 2744 (also known as AC118, or RXCJ0014.3-3022) at a redshift of $z = 0.308$ (Couch & Newell 1984). The $54\farcs3$ offset is $6\farcs9$ larger than that in the *Bullet Cluster* – although, as we shall discuss later, this value does not describe the separation of the main mass-clump from its stripped gas component. Nevertheless, Abell 2744 is undergoing a particularly interesting merger. The complex interplay between multiple dark matter and baryonic components appears to have unleashed 'ghost', 'dark', 'stripped' and 'bullet' clusters, and we dub the system *Pandora's Cluster*.

The first hint that Abell 2744 is in the middle of a major merging event arose from observation of a powerful and extended radio halo ($P(1.4\mathrm{GHz}) > 1.6 \times 10^{36}$ Watt, Giovannini et al. (1999); Govoni et al. (2001,?)). This indicated the presence of relativistic electrons accelerated through high Mach shocks or turbulence (e.g. Sarazin 2004). The picture was clarified by X-ray studies (Kempner & David 2004; Zhang et al. 2004) that revealed substructure near the cluster core, plus an additional luminous structure towards the Northwest. Kinematic observations of cluster member galaxies (Girardi & Mezzetti 2001) suggested a bimodal distribution in redshift space, but were not at first considered significant. Recent kinematic studies focussing solely on Abell 2744 definitely show a bimodal velocity dispersion in the cluster centre, together with a third group of cluster members near the Northwestern X-ray peak (Boschin et al. 2006; Braglia et al. 2009). Although there is no evidence for non-thermal X-ray emission (Million & Allen 2009), the fraction of blue star-forming galaxies (Braglia et al. 2007, and references therein) also seems to be enhanced. A default explanation emerged for the centre of Abell 2744, featuring a major merger in the North-South direction with a small inclination towards the line-of-sight and a $\sim$ 3:1 mass ratio of the merging entities (Kempner & David 2004; Boschin et al. 2006). More controversial is the role of the Northwestern structure. Kempner & David (2004) detected a cold front on its SW edge and a possible shock front towards the cluster core, so concluded that it is falling towards the main mass. More recent analysis of *Chandra* data (Owers et al. 2011) failed to confirm the presence of the shock front, only a cold front towards the Northern edge, and the authors proposed that the structure is moving instead towards the Northwest, away from the main cluster. What seems sure is that we are observing a complicated triple merger (Braglia et al. 2007).

Until now, Abell 2744 has been better constrained from X-ray and kinematic studies than by gravitational lensing. So far, Smail et al. (1997) detected a weak-lensing signal and strong-lensing features, followed by Allen (1998) who found a large discrepancy in the mass estimates for Abell 2744 from X-ray and strong-lensing reconstructions. Given the cluster's dynamical state, this finding is perhaps no longer surprising since the merging would induce non-thermal support and elongation along the line-of-sight, which increases the systematics from both methods. The most recent weak-lensing analysis (Cypriano et al. 2004) showed indications of substructure in the reconstructed surface-mass density, but did not reach the resolution required for more quantitative statements. Here, we present the results of an HST imaging survey, aimed at clarifying the evolutionary stage of this complex system.

This article is organised as follows. In Sec. 2 we present our comprehensive lensing analysis, mainly based on newly acquired data taken with the *Advanced Camera for Surveys (ACS)* on the *Hubble Space Telescope (HST)*. In Sec. 3 we describe a complementary X-ray analysis based on *Chandra* data. We discuss cosmological implications and an interpretation of the merging scenario in Sec. 4, and we conclude in Sec. 5. Throughout this paper we assume a cosmological model with $\Omega_\mathrm{m} = 0.3$, $\Omega_\Lambda = 0.7$ and $\mathrm{h} = 0.7$. At the cluster's redshift $z = 0.308$, one arcsecond corresponds to 4.536 kpc.

2 LENSING ANALYSIS

Our recently acquired, multiband *HST/ACS* imaging enables us to significantly improve upon previous mass models of Abell 2744. We have identified strong gravitational lensing of eleven background galaxies producing 34 multiple im-

ages around the Southern core, with an Einstein radius of $r_{\rm E} \sim 30''$ (see below). These enable us to tightly constrain the position and shape of the core mass distribution. No such multiple image systems are revealed around the N or NW clumps, immediately indicating that their masses are lower. Our *HST* images also yield ~ 62 galaxies/arcmin^2 for weak lensing analysis (after CTI corrections are performed, as described below). This enables detailed mass modelling throughout our *HST* field of view. To probe the cluster merger on even larger scales, we incorporate ground-based weak lensing measurements from *VLT* and *Subaru*.

We simultaneously fit all of these strong- and weak-lensing observations using our well-tested mass reconstruction algorithm (Merten et al. 2009; Meneghetti et al. 2010) (which is similar to that used by Bradač et al. (2006) and Bradač et al. (2008) to map the *Bullet Cluster* and the *Baby Bullet*). Importantly, we make no assumptions about mass tracing light in the combined analysis. Our analysis reveals *four* individual clumps of mass $\gtrsim 10^{14} M_{\odot}$ within a 250 kpc radius (figure 1). Previous weak lensing analysis of VLT images alone had resolved but a single broad mass clump (Cypriano et al. 2004). Below we describe our datasets, analyses, and results in more detail. The central cluster field and a preview on the matter and gas distribution is presented in Fig. 1.

2.1 The HST/ACS dataset

The *HST* data consist of two pointings in Cycle 17 (data taken between Oct. 27-30 2009, Proposal ID: 11689, P.I.: R. Dupke) with $\sim$ 50% overlap between the pointings. The images were taken with the *ACS/WFC* camera using three different filters, F435W (16.2 ksec[1]), F606W (13.3 ksec) and F814W (13.2 ksec).

The *HST/ACS* camera had been in orbit for eight years when the imaging was acquired. During this time above the protection of the Earth's atmosphere, its CCD detectors had been irreparably damaged by a bombardment of high energy particles. During CCD readout, photoelectrons are transported to the readout amplifier through a silicon lattice. Damage to this lattice creates charge traps that delay some electrons and spuriously trail the image – in a way that alters the shapes of galaxies more than the gravitational lensing signal that we are trying to measure. To undo this trailing and correct the `_raw` images pixel-by-pixel, we used the detector readout model of Massey et al. (2010), updated for device performance post Servicing Mission 4 by Massey (2010). The corrected data was then reduced via the standard CALACS pipeline (Pavlovsky 2006), and stacked using multidrizzle (Koekemoer et al. 2002).

2.2 Strong lensing

We concentrate our strong-lensing analysis on the reduced *ACS* images only. Several strong-lensing features are immediately identifiable by eye on the combined three-band image (Fig. 2). To find additional multiple images across the field of view, we apply the well-tested approach of Zitrin et al. (2009) to lens modelling, which has previously uncovered large numbers of multiply-lensed galaxies in *ACS* images of Abell 1689, Cl0024, 12 high-z MACS clusters, and MS1358 (respectively, Broadhurst et al. 2005; Zitrin et al. 2009, 2010a,b,c) .

In the Zitrin et al. (2009) method, the large-scale distribution of cluster mass is approximated by assigning a power-law mass profile to each galaxy, the sum of which is then smoothed. The degree of smoothing (S) and the index of the power-law (q) are the most important free parameters determining the mass profile. A worthwhile improvement in fitting the location of the lensed images is generally found by expanding to first order the gravitational potential of this smooth component, equivalent to a coherent shear describing the overall matter ellipticity, where the direction of the shear and its amplitude are free parameters. This allows for some flexibility in the relation between the distribution of DM and the distribution of galaxies, which cannot be expected to trace each other in detail. The total deflection field $\vec{\alpha}_T(\vec{\theta})$, consists of the galaxy component, $\vec{\alpha}_{gal}(\vec{\theta})$, scaled by a factor K_{gal}, the cluster DM component $\vec{\alpha}_{DM}(\vec{\theta})$, scaled by (1-$K_{gal}$), and the external shear component $\vec{\alpha}_{ex}(\vec{\theta})$:

$$\vec{\alpha}_T(\vec{\theta}) = K_{gal}\vec{\alpha}_{gal}(\vec{\theta}) + (1 - K_{gal})\vec{\alpha}_{DM}(\vec{\theta}) + \vec{\alpha}_{ex}(\vec{\theta}), \qquad (1)$$

where the deflection field at position $\vec{\theta}_m$ due to the external shear, $\vec{\alpha}_{ex}(\vec{\theta}_m) = (\alpha_{ex,x}, \alpha_{ex,y})$, is given by:

$$\alpha_{ex,x}(\vec{\theta}_m) = |\gamma| \cos(2\phi_\gamma)\Delta x_m + |\gamma| \sin(2\phi_\gamma)\Delta y_m, \qquad (2)$$

$$\alpha_{ex,y}(\vec{\theta}_m) = |\gamma| \sin(2\phi_\gamma)\Delta x_m - |\gamma| \cos(2\phi_\gamma)\Delta y_m, \qquad (3)$$

where $(\Delta x_m, \Delta y_m)$ is the displacement vector of the position $\vec{\theta}_m$ with respect to a fiducial reference position, which we take as the lower-left pixel position $(1, 1)$, and ϕ_γ is the position angle of the spin-2 external gravitational shear measured anti-clockwise from the x-axis. The normalisation of the model and the relative scaling of the smooth DM component versus the galaxy contribution brings the total number of free parameters in the model to 6. This approach to strong lensing is sufficient to accurately predict the locations and internal structure of multiple images, since in practice the number of multiple images readily exceeds the number of free parameters, which become fully constrained.

Two of the six free parameters, namely the galaxy power law index q and the smoothing degree S, can be initially set to reasonable values so that only 4 of the free parameters need to be fitted at first. This sets a very reliable starting-point using obvious systems. The mass distribution is therefore well-constrained and uncovers many multiple-images that can be iteratively incorporated into the model, by using their redshift estimation and location in the image-plane. At each stage of the iteration, we use the model to lens the most obvious lensed galaxies back to the source plane by subtracting the derived deflection field, then re-lens the source plane to predict the detailed appearance and location of additional counter images, which may then be identified in the data by morphology, internal structure and colour. We stress that multiple images found this way must be accurately reproduced by our model and are not simply eyeball "candidates" requiring redshift verification. The best fit is assessed by the minimum RMS uncertainty in the image plane

[1] Equally split between the two pointings

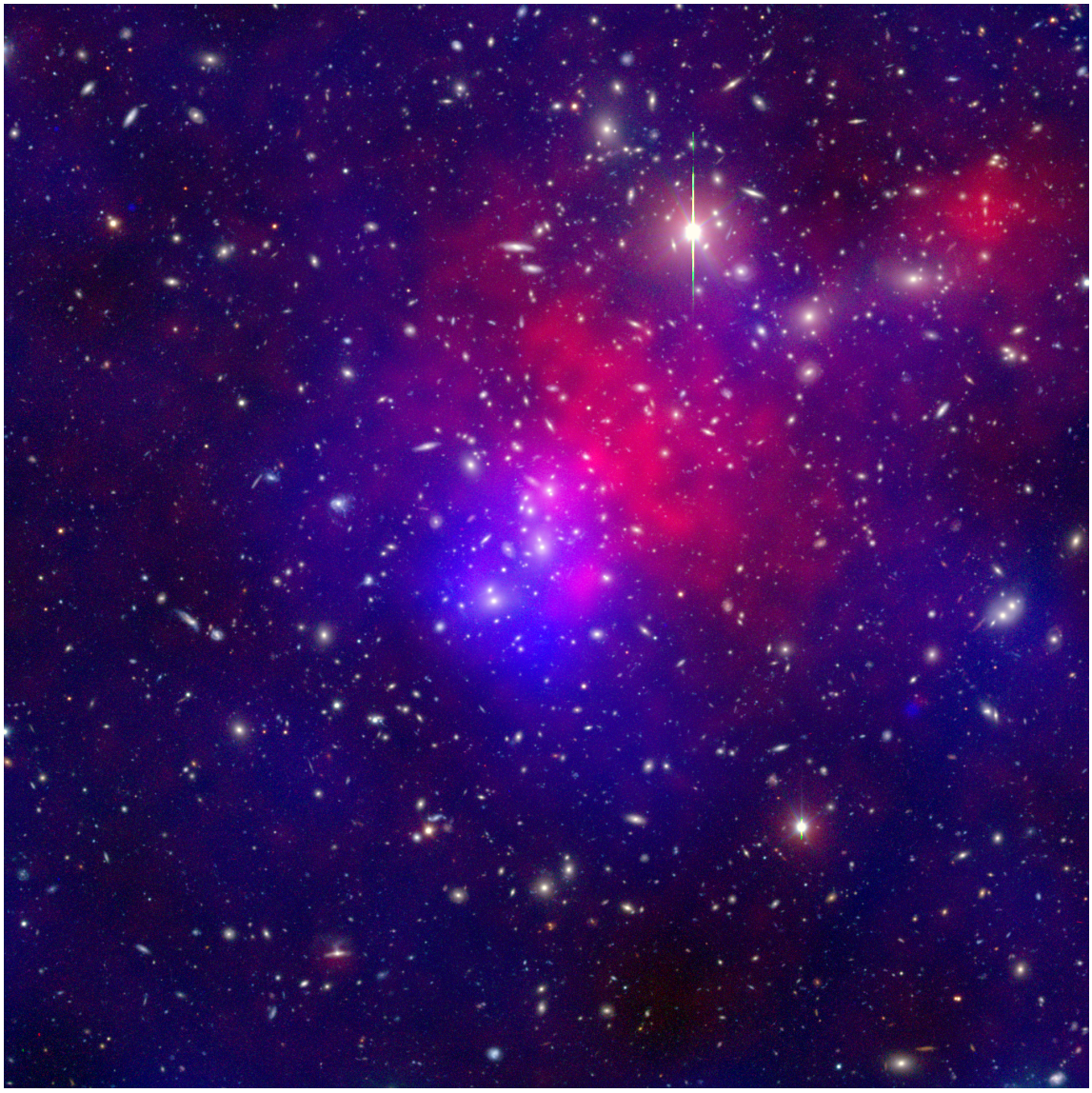

Figure 1. The central field of Abell 2744 as revealed by VLT VRI imaging. Overlaid in blue is the matter distribution, obtained by lensing and in red the X-ray luminosity in terms of phtoton counts. Brighter colours indicate a higher surface-mass density or X-ray brightness respectively. The field size is $403'' \times 403''$.

$$RMS^2_{\rm images} = \sum_i ((x_i^{'} - x_i)^2 + (y_i^{'} - y_i)^2) \; / \; N_{\rm images}, \quad (4)$$

where $x_i^{'}$ and $y_i^{'}$ are the locations given by the model, x_i and y_i are the real image locations, and the sum is over all $N_{\rm images}$ images. The best-fit solution is unique in this context, and the model uncertainty is determined by the locations of predicted images in the image plane. Importantly, this image-plane minimisation does not suffer from the well known bias involved with source plane minimisation, where solutions are biased by minimal scatter towards shallow mass profiles with correspondingly higher magnification.

In Abell 2744 we have uncovered a total number of 34 multiple images belonging to 11 background sources. We label the different systems in Fig. 2, which also shows the critical curve of the cluster derived from the strong lensing model. The model predicts an Einstein radius of $r_{\rm E} = 30'' \pm 3''$. With such a large number of clear multiple images we can constrain the inner mass distribution very well, and we shall incorporate these constraints into our joint strong- and weak-lensing analysis described in Sec. 2.4.

2.3 Weak lensing

Several areas outside the cluster core are of special interest, due to the complicated structure of this merging cluster. We measure the shapes of background galaxies to derive a weak-lensing signal and extend our mass reconstruction over the whole cluster field. Since our *HST* data cover only a limited field of view, we also include *VLT* and *Subaru* imaging in our weak lensing analysis.

Table 1. The multiple-image system of Abell 2744.

Image-ID (⟨source⟩.⟨image⟩⟨additional knot⟩)	x ($''$)	y ($''$)	z
1.1	−35.10	−13.55	2.0 ± 0.3
1.2	−30.15	−23.95	
1.3	0.10	−35.40	
1.11	−33.60	−16.50	
1.21	−31.50	−21.55	
1.31	1.60	−35.85	
2.1	9.30	−11.50	2.0 ± 0.3
2.2	−34.25	12.35	
2.3	2.80	1.05	
(2.4)	−0.50	−7.10	
2.11	11.55	−7.65	
2.21	−32.55	13.90	
2.31	5.55	3.10	
(2.41)	−0.05	−4.15	
3.1	−10.10	22.65	4.0 ± 0.3
3.2	−7.40	22.95	
(3.3)	27.15	2.20	
4.1	−18.25	−9.00	3.5 ± 0.3
4.2	−29.25	−5.30	
4.3	18.05	−31.60	
5.1	8.85	29.00	4.0 ± 0.5
5.2	3.85	31.60	
5.3	19.65	19.30	
6.1	−38.15	−5.95	3.0 ± 0.5
6.2	−24.25	−28.30	
6.3	−0.60	−33.15	
7.1	−37.35	−7.85	3.7 ± 0.5
7.2	−27.85	−26.10	
7.3	5.10	−34.85	
8.1	−10.70	20.90	4.0 ± 0.2
8.2	−8.00	21.40	
(8.3)	16.10	5.90	
9.1	−6.65	−18.45	3.0 ± 0.5
9.2	−2.80	−21.90	
(9.3)	−43.20	10.80	
10.1	−6.65	−20.65	3.0 ± 0.5
10.2	−3.55	−22.75	
10.3	−44.90	11.00	
(11.1)	−16.00	−13.30	3.0 ± 0.5
(11.2)	−34.20	−4.65	
(11.3)	10.70	−31.55	

If the image ID is shown in brackets, the image is not confidently reproduced by the lensing model described in Sec. 2.2. All other images define a 'confident catalogue' of multiple-image systems and are used in our subsequent analysis. The x-and y-coordinates are relative to the BCG position ($\alpha_{\rm J2000} = 3.58611$, $\delta_{\rm J2000} = -30.40024$) in arcseconds. Redshifts of each system and their respective error are derived from the model predictions.

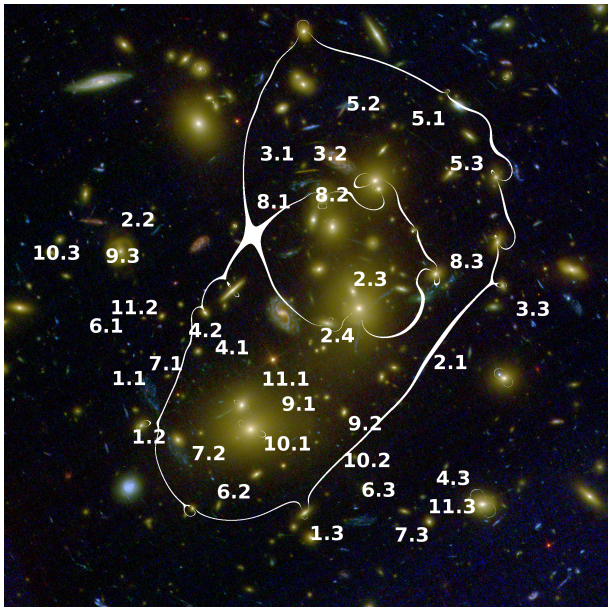

Figure 2. Shown as continuous white line is the critical curve of the cluster as it is derived from the strong-lensing model. It assumes a source redshift $z_{\rm S} = 2.0$. Also shown are the approximate positions of the identified multiple-image systems as they are listed in Tab. 1. The visible field size is $\sim 100'' \times 100''$.

2.3.1 HST/ACS

To select lensed background galaxies, we obtained rough photometric redshifts based on our three filters using BPZ (Benítez 2000; Coe et al. 2006). Cluster ellipticals at $z \sim 0.3$ occupy a unique region in our colour-colour space, enabling us to obtain better than expected results. Of 118 galaxies with published spectroscopic redshifts (Owers et al. 2011 and references therein; all $z < 0.7$) within our field of view, 99 yielded confident photo-z, and these proved accurate to $\Delta z \sim 0.06(1+z)$ RMS with no significant outliers. Background galaxies were selected as those with confident photo-z > 0.5.

We measure the weak gravitational lensing signal in the F814W HST exposures, which are the deepest and contain the most galaxies at high redshift. We measure the shapes of background galaxies, and correct them for convolution by the Point-Spread Function (PSF), using the 'RRG' (Rhodes et al. 2000) pipeline developed for the HST COSMOS survey (Leauthaud et al. 2007; Massey et al. 2007). The RRG method is particularly optimised for use on high resolution, space-based data. Since *HST* expands and contracts as it warms in the sun or passes through the shadow of the Earth, even this telescope does not have a constant PSF. However, 97% the variation in its PSF can be accounted for by variation in its focal length (Jee et al. 2007, the separation between the primary and secondary mirrors). We therefore measure its focal length by matching the shapes of the ~ 12 bright stars in each pointing to models created by raytracing through the optical design (Krist 2003). This achieves a repeatable precision of $1\mu m$, and we construct a PSF model from all those stars observed during the 600-orbit COSMOS survey at a similar focus (Rhodes et al. 2007) We finally use this PSF model to correct the shapes of galax-

ies, and to obtain estimates of the amount by which their light has been sheared. The result is a catalogue of 1205 galaxies with shear estimates, corresponding to a density of ~ 62 galaxies/arcmin^2.

2.3.2 VLT/FORS1

The complementary *VLT* data for our weak lensing analysis is identical to that included by Cypriano et al. (2004) in a study of 24 X-ray Abell clusters. The total field of view is $6\farcm8$ on a side, centred on the cluster BCG and significantly exceeding the coverage of our *HST* imaging. V, R and I-band imaging was obtained with the *FORS1* camera between April and July 2001, with exposure times of 330 s in each filter. The data were reduced with standard IRAF routines and, to maximise the depth, we perform weak-lensing shape analysis on the combined VRI image. Seeing conditions were excellent, with a FWHM of stars in the combined VRI image of $0\farcs59$.

We measure galaxy shapes and perform PSF correction using the `IM2SHAPE` method (Bridle et al. 2002). This involves a two-step process to first map the PSF variation across the observed field, then to model each detected galaxy, perform PSF correction and recover its ellipticity. To remove foreground contamination and unreliable shape measurements from our catalogue, we apply magnitude cuts plus additional rejection criteria (see Cypriano et al. 2004). Since that work, we have improved the efficiency of foreground galaxy removal and now keep a higher density of background galaxies in our shear catalogue. The result is a catalogue of 912 galaxies with shear estimates, or ~ 20 galaxies/arcmin^2.

2.3.3 SUBARU/SuprimeCam

To extend the total field-of-view even further, especially in the Northern areas of the cluster field, we obtained 1.68 ksec i'-band imaging data with *Subaru/SuprimeCam* during Semester S08B. The data were reduced following Okabe & Umetsu (2008) and Okabe et al. (2010a,b). Astrometric calibration was conducted by fitting the final stacked image with the 2MASS data point source catalog; residual astrometric errors were less than the CCD pixel size. Unfortunately, due to poor weather conditions, the seeing size is unfortunately as large as $1\farcs28$.

We measure galaxy shapes and perform PSF correction using the IMCAT package (provided by Kaiser et al. 1995) in the same pipeline as Okabe et al. (2010a,b) with some modifications following Erben et al. (2001). Background galaxies were selected in the range of $22 < i' < 26$ ABmag and $\bar{r}_h^* + \sigma_{r_h^*} \simeq 3.4 < r_h < 6.0$ pix, where r_h is the half-light radius, and $\bar{r}_h^*$ and $\sigma_{r_h^*}$ are the median and standard error of stellar half-light radii r_{h^*}, corresponding to the half median width of the circularised PSF. The density of background galaxies in our final shear catalogue is $\simeq 15$ arcmin^{-2}. This is 30-50% of typical values from images obtained during normal weather conditions Okabe et al. (2010a,b).

2.4 Combined lensing reconstruction

In order to combine the weak- and strong-lensing constraints in a consistent way, we use the joint lensing reconstruction algorithm described in Merten et al. (2009) (see also Bradač et al. 2005, 2009, for a similar approach). This method has been extensively tested in Meneghetti et al. (2010) and proved its capability to faithfully recover the cluster mass distribution over a broad range of scales.

Our joint mass reconstruction is nonparametric, in the sense that it neither makes any *a priori* assumptions about the cluster's underlying mass distribution nor does it need to trace any light-emitting component in the observed field. We reconstruct the cluster's lensing potential (its gravitational potential projected onto the plane of the sky) ψ by combining measurements of the position of the critical line and the reduced shear. To do this, we divide the observed field into an adaptive mesh, which discretises all observed and reconstructed quantities. A statistical approach is chosen to combine our various measurements, by defining a multi-component χ^2-function that depends on the underlying lensing potential and a regularisation term $R(\psi)$ to prevents the reconstruction overfitting noise (see Merten et al. 2009; Bradač et al. 2005)

$$\chi^2(\psi) = \chi^2_{\rm w}(\psi) + \chi^2_{\rm s}(\psi) + R(\psi). \quad (5)$$

The weak-lensing term is defined by the expectation value of the complex reduced shear in each mesh position $\langle\varepsilon\rangle$, which is obtained by averaging the measured ellipticities of all background galaxies within that grid cell

$$\chi^2_{\rm w}(\psi) = \left(\langle\epsilon\rangle - \frac{Z(z)\gamma(\psi)}{1-Z(z)\kappa(\psi)}\right)_i \mathcal{C}^{-1}_{ij} \left(\langle\epsilon\rangle - \frac{Z(z)\gamma(\psi)}{1-Z(z)\kappa(\psi)}\right)_j , \quad (6)$$

where $Z(z)$ is a cosmological weight factor as defined e.g. in Bartelmann & Schneider (2001), and $\gamma = \partial\partial\psi/2$ is the shear of the lens, with the two components expressed in complex notation. $\kappa = \partial\partial^*\psi$ is the convergence, where the complex differential operator in the plane is defined as $\partial := (\frac{\partial}{\partial\theta_1} + \mathrm{i}\frac{\partial}{\partial\theta_2})$, with θ_1 and θ_2 being the two angular coordinates in the sky. The indices i, j indicate the discretisation of the input data and the lens properties, where we have to take into account the full χ^2-function because the averaging process of background galaxies might result in an overlap of neighbouring mesh points, expressed by the covariance matrix $\mathcal{C}_{ij}$.

The strong-lensing term is defined as

$$\chi^2_{\rm s}(\psi) = \frac{(\det\mathcal{A}(\psi))^2_k}{\sigma^2_{\rm s}} = \frac{\left((1-Z(z)\kappa(\psi))^2 - |Z(z)\gamma(\psi)|^2\right)^2_k}{\sigma^2_{\rm s}} , \quad (7)$$

where the index k labels all pixels in the reconstruction mesh, which are supposed to be part of the critical curve within the uncertainties $\sigma_{\rm s}$, given by the pixel size of the grid. At these points, the Jacobian determinant $\det\mathcal{A}(\psi)$ of the lens mapping must vanish.

We iterate towards a best-fitting lens potential by minimising the χ^2-function at each mesh position

$$\frac{\partial\chi^2(\psi)}{\partial\psi_l} \stackrel{!}{=} 0 \quad \text{with} \quad l \in [0, ..., N_{\rm pix}] . \quad (8)$$

In practice, we achieve this by translating this operation into a linear system of equations and invoking a two-level iteration scheme (see Merten et al. 2009, and references therein).

In this analysis, we use all strongly lensed multiple-image systems from the confident sample (Tab. 1) together with their derived redshifts, and combine weak lensing shear catalogues from all three telescopes (see Sec. 2.3). The

HST/ACS and *VLT/FORS1* shear catalogues are simply merged and together cover a field of $\sim 400'' \times 400''$. To extend the field to $600'' \times 600''$, centred on the BCG, we add the *Subaru* catalogue. Due to the poor seeing conditions during this exposure and due to the unreliable background galaxy selection from a single passband, we exclude the central part of the field already covered by *HST* and *VLT*, and also limit the total field size to the central part of the *SuprimeCam* image. The combination of strong lensing data and the density of background galaxies allows for a reconstruction on a mesh of 72×72 pixels in the central region (corresponding to a pixel-scale of $8.4''$/pix) and 36×36 pixels in the outskirts of the field (corresponding to a pixel-scale of $16.7''$/pix). Error estimates were produced by bootstrapping the redshift uncertainties of the strong-lensing constraints, with 500 bootstrap realisations of the refined cluster core, and by directly bootstrapping the combined ellipticity catalogue, providing 150 bootstrap realisations of the cluster outskirts. The number of bootstrap realisations is mainly constrained by runtime considerations. All error estimates are calculated such that 68% of the bootstrap realisations fall into the given error interval.

2.5 Reconstruction results

We obtain a map of the lensing convergence across the field (proportional to the projected mass) by applying the Laplacian operator to the the lensing potential on the adaptively refined mesh (see Fig. 3). We find a total mass within a radius of 1.3 Mpc around the Core of $M(r < 1.3\mathrm{Mpc}) = 1.8 \pm 0.3 \times 10^{15} M_{\odot}$, which is in good agreement with kinematically derived masses (Boschin et al. 2006). A mass determination within a field of (1300×750) kpc centred on the Core density peak yields $M(1.73\mathrm{Mpc}^2) = 8.3 \times 10^{14} M_{\odot}$, rendering Abell 2744 comparable in mass or slightly less massive than the *Bullet Cluster* (Bradač et al. 2006). The overall radial convergence and mass profile can be found in Fig. 4.

Most interestingly, our gravitational lensing analysis resolves four distinct sub-structures, indicated in Fig. 3 by the white circles. We label these substructures as Core, Northwestern (NW, later on dubbed as 'dark'), Western (W, later on dubbed as 'stripped') and Northern (N) structure. The positions of the mass peaks and their local projected masses within 250 kpc are listed in Tab. 2. The new *HST/ACS* images thus allow a striking improvement in our map of the mass distribution and reveal the distribution of dark matter sub-structure in great detail for the first time. We will refer to the individual mass clumps resolved here in our discussion of the X-ray analysis below.

3 X-RAY ANALYSIS

The most difficult part of interpreting merging clusters is determining the geometric configuration of the collision, such as its impact velocity, impact parameter and angle with respect to the plane of the sky (Markevitch et al. 2002). For this purpose, X-ray data becomes a crucial addition to lensing measurements. The location of any shock fronts are revealed in the temperature of the intracluster medium (ICM). Velocities can be inferred from the density and temperature of intracluster gas (if the merger axis is near the plane of the sky), or through direct Doppler measurements (if the merger axis is near the line of sight).

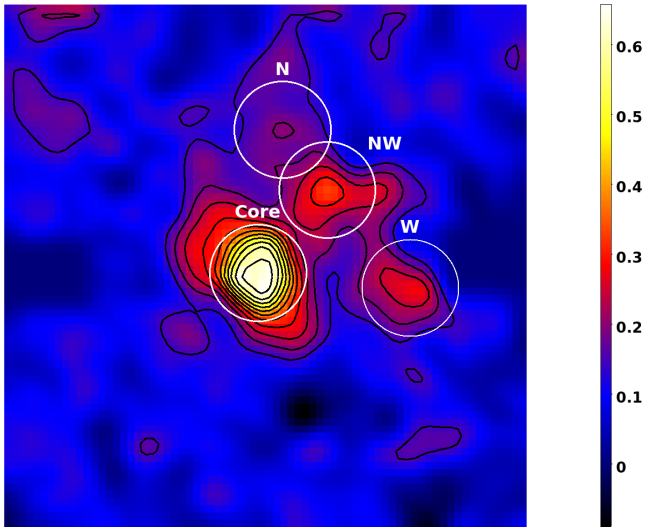

Figure 3. The convergence map of the cluster field for a source redshift of $z_S = \infty$ and a field size of $600'' \times 600''$. The black contours start at $\kappa_0 = 0.14$ with a linear spacing of $\Delta\kappa = 0.047$. The four white circles with labels indicate identified sub-clumps and the radius within which their mass is calculated. The radius of all four circles is $55.4'' \approx 250$ kpc.

Table 2. Structures identified within our lensing reconstruction.

Name	x ($''$)	y ($''$)	Δpos ($''$)	$M(r < 250\mathrm{kpc})$ ($10^{14}\ M_{\odot}$)
Core	-8.06	-8.06	10.6	2.31 ± 0.17
NW	71.4	87.0	15.0	1.24 ± 0.16
W	166.1	-25.4	15.0	0.98 ± 0.25
N	20.1	156.0	15.0	0.93 ± 0.17

The x-and y-coordinates are provided in arcseconds, relative to the BCG position ($\alpha_{\mathrm{J2000}} = 3.58611$, $\delta_{\mathrm{J2000}} = -30.40024$). The 68% confidence limits on peak positions are derived from 500 bootstrap realisations for the Core peak, and from the pixel size of the coarse weak lensing mesh in the reconstruction outskirts for the other mass peaks. Masses assume $h = 0.7$ and their 68% confidence limits are derived from bootstrap realisations as described in the text.

3.1 Reduction of the *Chandra* data

We reanalyse all existing *Chandra* data of Abell 2744 (listed in Owers et al. (2011)), using CIAO 4.2 with the calibration database CALDB 4.3.0. We clean the data using the standard procedure[2] and keep events with grades 0, 2, 3, 4 and 6. We remove the *ACIS* particle background as prescribed for 'VFAINT' mode, and apply gain map correction, together with Pulse Hight Amplitude (PHA) and pixel randomisation. Point sources are identified and removed, and the sky

[2] http://cxc.harvard.edu/ciao/guides/acis_data.html

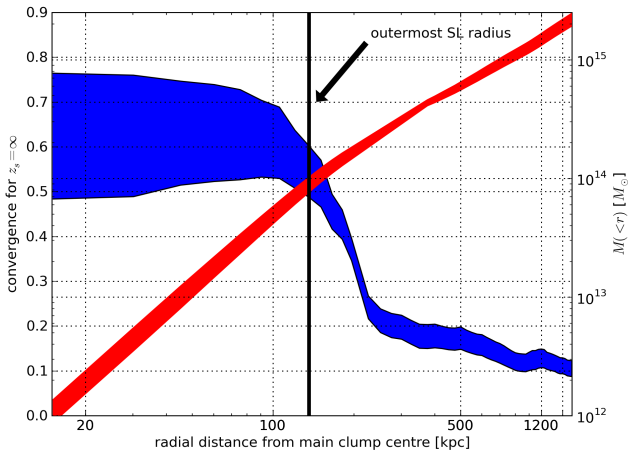

Figure 4. Radial mass profiles of the cluster, derived from our lensing analysis. Shown in blue (referring to the left y-axis) is the convergence profile for a source redshift $z_s = \infty$. The large uncertainty for small radii arises from uncertainty in the exact position of the cluster centre. The cumulative mass as a function of radial distance from the cluster centre is shown in red (referring to the right y-axis). The black vertical line indicates the distance of the outermost multiple images from the cluster centre.

background to be subtracted from spectral fits is generated from Blank-Sky observations using the `acis_bkgrnd_lookup` script. We fit spectra using XSPEC V12.5.1n (Arnaud 1996), which allows the abundances of several elements to be measured simultaneously; we adopt VAPEC thermal emission models from atomic data in the companion Astrophysical Plasma Emission Database (Smith et al. 2001). Galactic photoelectric absorption is incorporated using the `wabs` model (Morrison & McCammon 1983). Spectral channels are grouped to have at least 20 counts/channel. Energy ranges are restricted to 0.5–9.5 keV. Metal abundances are quoted relative to the solar photospheric values of Anders & Grevesse (1989), and the spectral fitting parameter errors are 1-σ unless stated otherwise.

There is a known reduction of quantum efficiency at energies below 1 keV due to a build-up of molecular contaminants on the optical blocking filter (or on the CCD chips)[3]. To prevent this affecting our measurement of low energy line abundances, hydrogen column density and overall gas temperature, we fix the column density to the cluster's nominal value of 1.6×10^{20} cm^{-2} (Dickey & Lockman 1990). This correction is now done automatically within the `mkwarf` routine. To be conservative, we present results from only those regions of the CCDs best-suited for velocity analysis (*ACIS-I* pointings 8477 and 8557); for an independent sanity check, we also repeat the analysis with *ACIS-S* pointing 2212. We exclude pointings 7712 and 7915 because the regions of interest cross multiple CCDs, and interchip gain fluctuations could introduce spurious systematic effects.

Since spectral models are (weakly) degenerate with cluster redshift, it is common for simultaneous fitting routines to get stuck in local χ^2 minima before they reach the global best fit. We circumvent this via an iterative approach. We perform initial fits while varying both the spectral model and redshift values within reasonable ranges (via the command STEPPAR in XSPEC). We then fix the redshift, and refit full spectral models to infer gas temperature, metal abundances and normalisations. Subsequently, we use these models as inputs in a new fit with the redshift free to vary. This provides an error on the redshift measurement, and may also yield a better-fit redshift. We repeat the process until the best-fit redshift no longer changes between iterations.

3.2 Previous X-ray observations & interpretations

Abell 2744 shows an extremely disturbed X-ray morphology. With 25 ksec of *Chandra ACIS-S3* imaging, Kempner & David (2004) decided it is the aftermath of a N-S collision between similar mass proto-clusters, at Mach > 2.6. They also found tentative evidence for a cold front in the detached nearby NW 'interloper', which they guessed was falling into the main cluster. Owers et al. (2011) obtained a further 101 ksec of *ACIS-I* imaging. The deeper data revealed the 'Southern minor remnant core' (SMRC) to be colder ($T_X \sim 7.5$ keV) than its surroundings, with a high temperature region to the SE ($T_X > 15$ keV) that they interpreted as a shock front. They concluded the SMRC had been a low-mass bullet that has passed through the 'Northern major remnant core' (NMRC), leaving central tidal debris (CTD). The pressure ratio of $\sim$ 3:1 across the shock front corresponds to a sky-projected shock velocity of 2150 km/s (for an average temperature T_X ~8.6 keV). Owers et al. (2011) reversed the Kempner & David (2004) model of the interloper, concluding that it came originally from the South, has already passed through the main body of the host cluster with a large impact parameter, and is now climbing out towards the N-NW.

Owers et al. (2011) also obtained spectra of more than 1200 galaxies with the *Anglo-Australian Telescope* multi-fibre *AAOmega* spectrograph, and confirmed the velocity bi-modality of the cluster galaxies. One component of galaxies near the SMRC has a peculiar velocity of 2300 km/s; a separate component near the NMRC has a peculiar velocity of about -1600km/s and enhanced metal abundances ($\sim$ 0.5 Solar). Assuming that the Northern and Southern cores have the same velocities as the 'apparently' associated galaxy populations, they de-projected the velocity of this collision to Mach 3.31 or nearly 5000 km/s.

An interesting prediction of this scenario is that the intracluster gas should show a strong radial velocity gradient of $\sim$ 4000 km/s or $\Delta\ z \sim 0.014$ from North to South. Since the intracluster medium is enriched with heavy elements, radial velocity measurements could be carried out by measuring the Doppler shift of emission lines in the X-ray spectrum (Dupke & Bregman 2001b,a; Andersson & Madejski 2004; Dupke et al. 2007) or through changes in line broadening due to turbulence (Inogamov & Sunyaev 2003; Sunyaev et al. 2003; Pawl et al. 2005). The former requires high photon counts within the spectral lines and excellent control of instrumental gain but could, in principle, be measured with current X-ray spectrometers. The latter requires very high spectral resolution that should become available

[3] http://cxc.harvard.edu/cal/Links/Acis/acis/Cal_prods/qeDeg/index.html

through the future *ASTRO-H* and *IXO* satellites (however, see Sanders et al. 2010, 2011). The existing data are not ideal for high precision measurements of ICM velocity structure, but we shall test for consistency with the proposed merger configuration. *Chandra* has a good gain temporal stability (Grant 2001) and we shall control for spatial variations by performing resolved spectroscopy of multiple cluster regions using *the same CCD location* in different *ACIS-I* pointings.

3.3 Velocity measurements

We perform our analysis twice: for the regions of interest defined by Owers et al. (2011), then for the substructures prominent in our lensing mass maps. These are respectively indicated by green or blue circles in Fig. 5.

We find temperature and metal abundance values for the NMRC, CTD and SMRC of 7.3±0.64 keV and 0.63±0.18 Solar (χ_ν = 1.32 for 229 degrees of freedom); 8.72±0.47 keV and 0.27±0.08 Solar (χ_ν = 1.09 for 460 degrees of freedom); and 7.69±0.86 keV and 0.81±0.35 Solar (χ_ν = 1.01 for 143 degrees of freedom). These values are derived from simultaneous fits to pointings 8477, 8557 and 2212. However, there is a 10% enhancement in temperature and a $>$ 20% enhancement in metal abundance when the *ACIS-S* observation is excluded, and this is not due to different levels of contaminants on the CCDs. The same difference is apparent if the two *ACIS-I* exposures are fitted individually. The reason for this discrepancy is not clear but it was also noted in Owers et al. (2011) (Owers, M. Personal Communication). Given that the observations were not tailored for velocity measurements (*i.e.* we cannot exclude temporal or inter-chip gain variations), we conservatively include in our error bars secondary χ^2 minima that are separated from the global minimum at less than 90% confidence in all measurements. Our temperature and abundance measurements are thus consistent with the values found by Owers et al. (2011).

Our velocity measurements are consistent with the presence of a gradient between the NMRC and SMRC, but in the opposite sense to that expected from the Owers et al. (2011) interpretation. Using only the observations (8477 and 8557) with identical CCDs, we find a velocity difference between NMRC and SMRC of $>$ 2650 km/s at 90% confidence. The *ACIS-S* observation (2212) cannot constrain the velocity gradient by itself (*i.e.* the data is consistent with zero km/s at the 90% confidence) but, when jointly fitted with the other two pointings, indicates a velocity gradient between NMRC and SMRC of $>$ 5300 km/s at 90% confidence. Therefore, although our analysis is consistent with a high velocity gradient, the direction of the gradient does not corroborate the merger configuration suggested by Owers et al. (2011).

We also measured the line-of-sight gas velocity in two new regions of interest (Core and NW) from our lensing mass reconstruction. Using all three exposures, we measure their gas temperatures and metal abundances to be $T_{X_{Core}}$=9.18±0.57 keV, A_{Core}=0.31±0.11 Solar with a reduced chi-squared χ_ν=1.08 for 461 degrees of freedom and $T_{X_{NW}}$=9.24±0.54 keV, A_{NW}=0.41±0.09 Solar with χ_ν=1.06 for 474 degrees of freedom. Despite their similar gas properties, these regions show a velocity gradient $>$ 4900 km/s at near 90% confidence, even including typical (1σ) intra-chip gain variations of 750 km/s (e.g. Dupke & Bregman 2006) in the error budget. A contour plot of the velocity difference is shown in Fig. 6. This result is consistent with new idea that the Southern Core mass is *redshifted* with respect to other structure. Nonetheless, these calculations should be taken with caution due to the uncertainties related to temporal gain variations and inter-chip gain variations between *ACIS-I* and *ACIS-S*. The same analysis using only with the *ACIS-I* observations shows the same velocity trend, but with a significant reduction in the absolute velocity difference (an upper limit of ∼2300 km/s at 90% confidence). Deeper *Chandra* observations, specifically tailored for velocity measurements, are now crucial to further reduce uncertainties and to better constrain the velocity structure of this cluster.

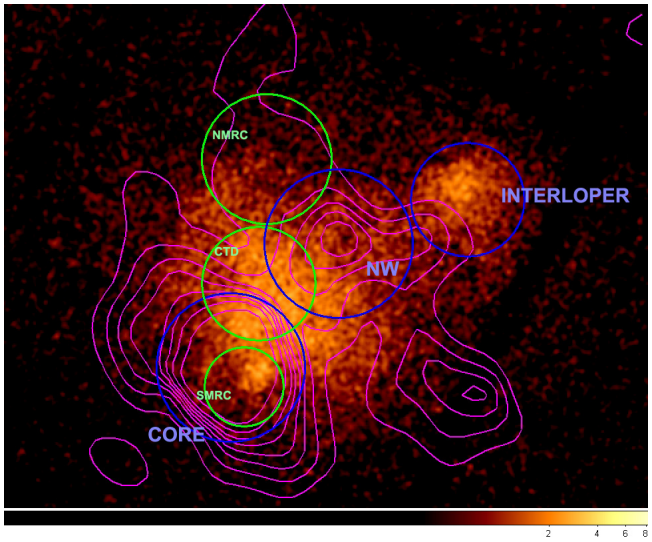

Figure 5. X-ray image of Abell 2744, overlaid with our lensing mass reconstruction (magenta). The velocity gradient is maximal between three regions of interest named by Owers et al. (2011) and circled in green (Southern minor remnant core, Northern major remnant core, and Central tidal debris). A velocity gradient is also detected between the regions of interest from our lensing mass reconstruction, circled in blue (Core and NW) as well as the interloper.

4 INTERPRETING THE MERGER

Abell 2744 is undoubtedly undergoing a complicated merging process on a large cluster scale. Progressively more detailed studies, culminating in our lensing reconstruction (Sec. 2) and X-ray analysis (Sec. 3), have only agreed that the merger is more complex than previously thought. For example, the likely explanation for the gas velocity gradient in the opposite direction to that expected by Owers et al. (2011) is that the NMRC is *not* the main cluster. Our lensing mass reconstruction shows that the deepest gravitational potential is by far the Southern 'Core' structure, which is roughly coincident with Owers et al.'s SMRC but slightly further offset from the Compact Core. We also find three separate mass concentrations to the North, Northwest and West. Overlaying the lensing mass reconstruction and X-ray emission (Fig. 7) reveals a complex picture of separations between the dark matter and baryonic components (quantified

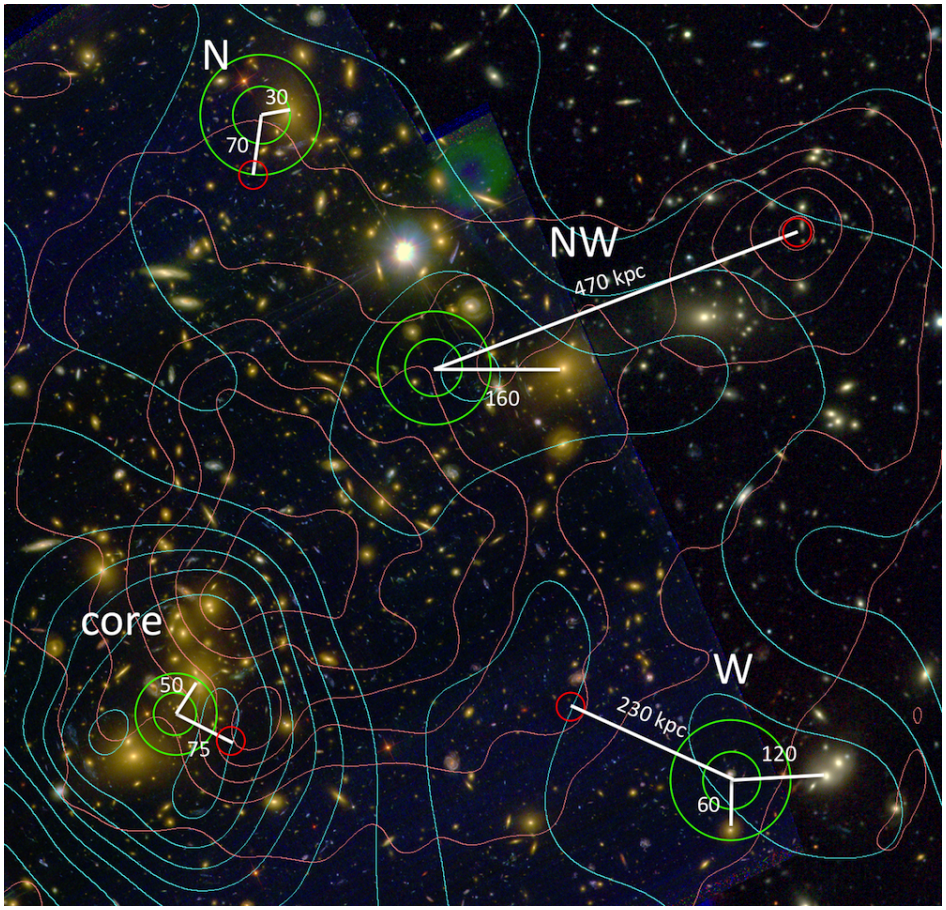

Figure 7. The different merging bodies in the field of Pandora's cluster. The false-colour background is provided by *HST/ACS*, *VLT* and Subaru images on a field size of $240'' \times 240''$. Overlaid in cyan are the surface-mass density contours and in magenta the X-ray luminosity contours. The positions of the dark matter clumps are indicated by the green annuli, showing also an aggressive and a conservative error estimate on these positions. The red circles show the position of the local overdensities in the gas distribution , associated to each individual dark matter clump. The white rulers show the separation between dark matter peaks and the bright clusters galaxies and local gas peaks.

Table 3. Separations between dark matter and baryonic components in the four regions of interest found by our lensing mass reconstruction.

mass peak	DM-gas separation ($''$)	DM-light separation ($''$)
Core	17 ± 10	10 ± 10
N	15 ± 10	7 ± 10
NW	103 ± 10	36 ± 10
W	~ 50	26 ± 10

in Tab. 3). To interpret the sequence of events that led up to this present state, we shall now tour the regions of interest, with more detailed discussions.

4.1 Core, the massive clump

According to our lensing analysis, the Core region (lower-left quadrant of Fig. 7) is by far the most massive structure within the merging system (*c.f.* Tab. 2). All the strong lensing features can be seen within this clump. We find no large separation between the distribution of mass and baryonic components. The mass peak is centred amongst the bright cluster member galaxies (within 1σ errors, it is consistent with the position of the BCG) and only 17 ± 10 arcseconds from a peak of X-ray emission identified by Owers et al. (2011). We support the general conclusion of Owers et al. (2011) that the major-merger in Abell 2744 is similar to that of the *Bullet Cluster* as it would be seen at a large inclination with respect to the plane of the sky. However, we reverse the ordering of the major and minor mass components.

One can infer constraints on the collisional cross-section of dark matter from the separation between peaks in the lensing and X-ray maps. For the *Bullet Cluster*, (Markevitch et al. 2004) found $\sigma/m < 5$ cm^{2}g^{-1}, and for the *Baby Bullet*, (Bradač et al. 2008) found $\sigma/m < 4$ cm^{2}g^{-1}. In the Core of Abell 2744, we observe a projected $17''$ separation that, if the inclination is $\sim 30^\circ$ away from the line-of-sight (Owers et al. 2011), is a physical separation similar to that in the other bullet clusters. For an order of magnitude analysis, we measure the mean surface-mass density within 150 kpc of the mass peak $\Sigma \simeq 0.31 \pm 0.05$ g cm^{-2}, so that the scattering

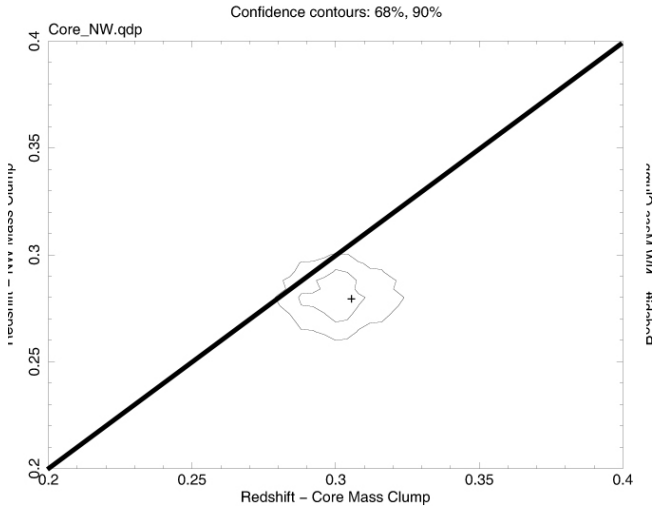

Figure 6. Simultaneous fits to the redshifts of the Core region and the NW substructure using two *ACIS-I* and one *ACIS-S* pointings. The two contours correspond to 68% (inner) and 90% (outer) confidence levels, and the diagonal line indicates equal redshifts to guide the eye.

depth $\tau_S = \sigma/m\ \Sigma$. With the assumption $\tau_s < 1$, which is justified due to the observed dark matter-gas separation, we deduce $\sigma/m < 3\ \mathrm{cm}^2\mathrm{g}^{-1}$. This system may therefore yield the tightest constraints on the interaction cross-section of dark matter, based on such analyis. A full numerical simulation to interpret the cluster configuration would be ideal, especially given uncertainty in the collision angle with respect to the plane of the sky. Indeed, even tighter constraints ($\sigma/m < 0.7\ \mathrm{cm}^2\ \mathrm{g}^{-1}$) were obtained from the *Bullet Cluster* by (Randall et al. 2008), who interpreted the offsets between all three cluster components via tailored hydrodynamical simulations. Additional constraints on the collisional cross-section have also recently been obtained from dark matter stripping in Abell 3827 (Williams & Saha 2011; Carrasco et al. 2010) and the ellipticities of dark matter halos (Feng et al. 2010; Miralda-Escudé 2002).

4.2 Northern, the bullet

Our analysis of the Northern mass substructure (upper-left quadrant of Fig. 7) confirms the overall North-South merging scenario proposed by several authors in the past. We find a mass ratio of ~ 2.5 between the Core and the Northern clump, roughly supporting the 3:1 merging scenario of Boschin et al. (2006), but we identify the Northern subclump as the less massive progenitor. This conclusion is robust, with no strong lensing features revealed by even our high resolution *HST* imaging in the Northern structure, as would have been expected for the reversed mass ordering proposed by Owers et al. (2011).

X-ray emission in the Northern mass substructure lags behind the dark matter as expected. We measure a separation of $\sim 15''$ to the South. This is a similar separation to that in the core but, due to the lower surface-mass density in this region, constraints on the collisional cross-section are less significant.

4.3 Northwestern, the ghostly and dark clumps

By far the most interesting structure is located to the Northwest of the cluster field (upper-right quadrant of Fig. 7). Our lensing analysis (Sec. 2.5) shows it to be the second-most massive structure. A separate region of X-ray emission also lies to the Northwest, called the NW interloper by Owers et al. (2011). However, the separation between our NW mass peak and the NW interloper is huge ($\sim 100'' = 470$ kpc). With a de-projected temperature of ~ 5 keV (Owers et al. 2011) the NW interloper should have $r_{500} \sim 1.34$ Mpc, (Evrard et al. 1996) and $M_{500} \sim 4-5\times10^{14} M_\odot$ (*e.g.* Fig. 8 of Khosroshahi et al. (2007)). Its $0.1-10.0$keV unabsorbed luminosity is 2.5×10^{44} erg/s, consistent with its gas temperature of $4-5$ keV (Khosroshahi et al. 2007; Díaz-Giménez et al. 2011). Assuming a β (from a King-like profile) of 0.67, typical for clusters, the clump would have $\sim 0.95\times10^{14} M_\odot$ within within 250 kpc, similar to the N clump, and should have been easily detected in the lensing analysis. The interloper thus appears to be an X-ray feature with no associated dark matter or galaxies, and we therefore dub it the 'ghost' cluster.

There is also a clear separation between the peak of the NW mass clump and any cluster member galaxies, so we call this the 'dark' cluster. Contours of the lensing mass reconstruction extend towards the West, where indeed we find a pair of BCGs (see Fig. 7). However, with the limited resolution of the *VLT* weak lensing reconstruction, it is impossible to tell whether this is a binary mass structure.

The separation between all three mass components makes this a real puzzle. One possible explanation was suggested by Owers et al. (2011), who describe it as a ram-pressure slingshot (e.g. Markevitch & Vikhlinin 2007). In this interpretation, after first core-passage, gas initially trails its associated dark matter but, while the dark matter slows down, the gas slingshots past it due to a combination of low ram-pressure stripping and adiabatic expansion and cooling, which enhances the cold front temperature contrast (Bialek et al. 2002). There is indeed a clear velocity gradient between the NW interloper and the main cluster core (see Sec. 3). Such effects have also been observed e.g. in Abell 168 (Hallman & Markevitch 2004) and in numerical simulations (Ascasibar & Markevitch 2006; Mathis et al. 2005), although at a much smaller separations between dark matter and gas. The more than $100''$ separation in Abell 2744 suggests either that the slingshot scenario is unlikely or that some amplifying mechanism is in place. We shall return to this issue, proposing an interpretation of the entire cluster merger, at the end of this section.

4.4 Western, the stripped clump

The Western substructure (lower-right quadrant of Fig. 7) has not yet been discussed in the literature, but several cluster member galaxies are found in this area. We find a prominent weak gravitational lensing signal of $\sim 1.0\times10^{14} M_\odot$ within 250 kpc. This should correspond to an X-ray brightness higher than the NW interloper, for the same gas temperature. However, we detect no X-ray emission. The best X-ray data (*ACIS-I* pointings 8477 & 8557) do not cover the region of this lensing signal, but the *ACIS-S* pointing 2212 indicates no excess diffuse gas above the cosmic background

and the extended tail of the cluster's outskirts. To match these observations, the Western clump must have been completely stripped of its ICM, so we dub it the 'stripped' clump.

The only slight excess X-ray emission nearby is a faint extension of the main cluster core towards the West ('ridge c' in Owers et al. 2011). This roughly links the Western clump to the Northern clump, and is consistent with remnants stripped by ram-pressure during a secondary merging event (NE–SW), almost perpendicular to the main merging event projected in the sky plane. To quantify the excess X-ray emission, we measure counts inside three equal-size, non-overlapping regions extending from the cluster core to a radial distance of $150''\approx 680$ kpc, as shown in Fig. 8. To prepare the data for this analysis, we divide the image by the exposure map following the standard procedure, remove hot pixels and remove point sources using the `dmfilth` routine in CIAO. We find a marginal excess in the central box (1030±32 counts), which points to the Western clump, above the Northern (965±31 counts) and Southern (876±29 counts) boxes. The cluster's surface brightness profile from the core towards the Western clump (along the central box) is shown in Fig. 9. The slope of the profile changes $\sim 135''=612$ kpc from the centre, becoming significantly shallower. If we take that point of transition as the location of the remaining gas core, we obtain a separation between the gas and dark matter of $30''$. Similar results are found with the shallower observation 7915 using *ACIS-I*.

We find a slight offset between the peak of the lensing mass reconstruction and the most luminous nearby cluster member galaxies. However, there is large uncertainty in the position of the lensing peak because this lies outside the *HST* imaging area. Our weak lensing analysis uses only *VLT* imaging, and there are no strong lensing constraints, so the mass reconstruction has a broad central plateau. Additional *HST* observations would provide an ideal foundation to better understand the Western area, which turns out to be playing a significant role in the overall merger.

4.5 One possible interpretation

We shall now try to develop a possible explanation of the complex merging scenario that has taken place in Abell 2744. To recap, we find four mass clumps (Core, N, NW, W) with approximate masses 2.3, 1, 1.25, $1\times10^{14}M_\odot$,respectively. The Core, N and W clumps are relatively close to BCGs and hot gas. The NW structure, on the other hand, contains separated dark matter, gas and galaxies.

We propose that the current configuration is the result of a near simultaneous double merger, as illustrated in Fig. 10. The first merger, in the NE-SW direction, had a characteristic path of $208''$ (plane of the sky distance between N and W clumps) or $\sim$ 0.95 Mpc (assuming no line of sight velocity component). The Western clump probably passed closest through the main cluster, as it had its ICM ram-pressure stripped completely. The second merger, in the SE-NW direction, had a characteristic path of $117''/\sin(27^\circ)\approx 1.17$ Mpc, if we assume the inclination of that merger suggested by Owers et al. (2011) of 27°. The mergers happened around 0.12–0.15 Gyr ago, with a characteristic velocity of $\sim$ 4000 km/s as indicated by the galaxy velocity difference and the ICM gas velocity measurements.

It is possible that the merger in the SE-NW direction could even have consisted of three initial substructures: the Core and two consecutive clumps (with a combined mass of $1.2\times10^{14}M_\odot$) falling along a filament. Those smaller clumps would be accelerated by the gravitational pull of the main cluster (plus the Northern and Western clumps, which were merging perpendicularly). The ram-pressure slingshot in these clumps could be enhanced by a combination of an initially stronger gravitational field and perhaps a posterior reduction in ram-pressure due to the 'puff-up' of the gas density due to the recent merger of Core+N+W, similar to the

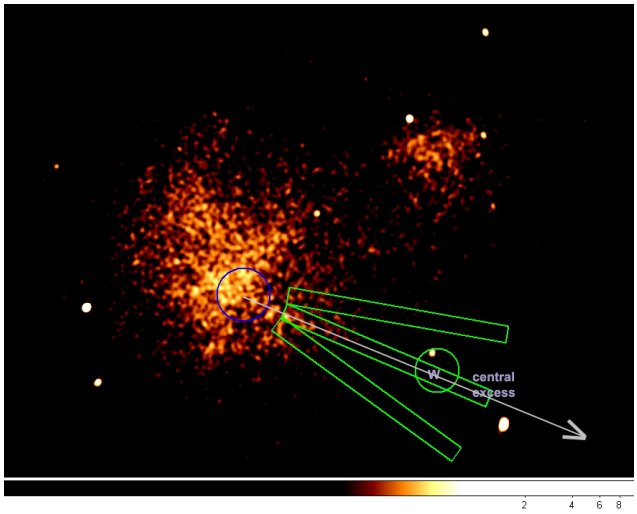

Figure 8. *Chandra ACIS-S3* X-ray image of Abell 2744, smoothed with a 3 pixel kernel Gaussian. We analyse the cluster's X-ray profile in three rectangular regions, each $150''$ in length and radiating from the cluster centre (marked by the blue circle). We find marginally significant excess X-ray emission in the central rectangular region, which extends towards the Western clump (marked by the green circle).

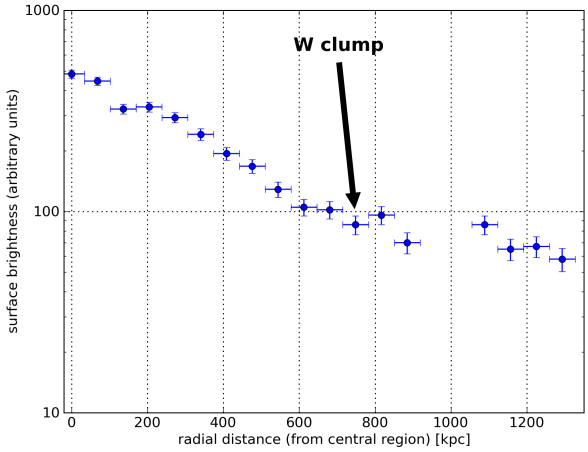

Figure 9. Surface brightness profile (in arbitrary units) of the central rectangular region shown in Fig. 8. The left hand side starts at the X-ray centre, and the arrow denotes the approximate position of the Western mass clump. The abrupt change in profile slope at roughly the same location is highlighted by the intersection with the horizontal line.

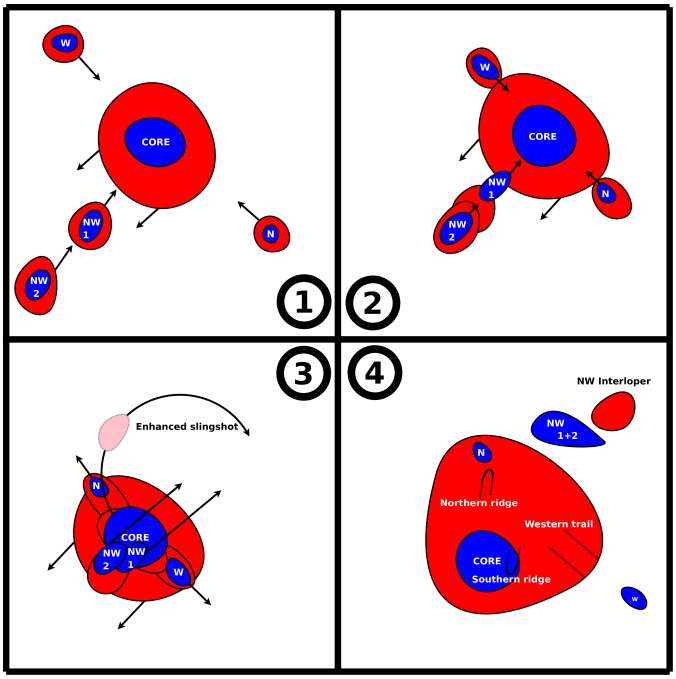

Figure 10. Our proposed merging scenario, illustrated in time-ordered sequence, to explain the current configuration (panel 4). We suggest that Abell 2744 is the result of a near simultaneous double merger: one in the NE-SW direction and another in the NW-SE direction, which may even have consisted of three separate structures falling along a filament. Blue colour shall indicate the innermost dark matter cores of the clumps, where else their respective ICM is shown in red.

density configuration of the main component in the *Bullet Cluster*. The combined effect would throw the gas component ahead of its associated dark matter, forming the 'ghost' cluster, which is now the interloper. The two dark matter clumps left behind would now form the double-centred 'dark' clump.

This spectacular scenario seems plausible and fits the current observations. However, the interloper has not been covered by the current HST observations and that the Western clump falls between chip gaps in the longer Chandra exposures, so further observations will still be required. Our suggestions will also eventually require verification via a set of well-tailored numerical simulations and have to be taken with some caution at the current stage.

5 CONCLUSIONS

We present a detailed strong lensing, weak lensing and X-ray analysis of the merging cluster of galaxies Abell 2744. Earlier studies (Kempner & David 2004; Boschin et al. 2006; Braglia et al. 2009; Owers et al. 2011) concluded that Abell 2744 is undergoing a complicated merging event. We find that it is even more complex than previously thought.

Deep, three-band *HST*-imaging reveals a variety of strong-lensing features in the core of the cluster. From our comprehensive strong-lensing modelling of the central mass distribution, we identify a total number of not less than 34 multiple images, in 11 multiple-image systems, together with their respective redshifts. The strong lens systems are listed in Tab. 1 and the finely resolved critical curve of the cluster core is shown in Fig. 2. The Einstein radius of the core is $r_E = 30'' \pm 3''$.

We extended the strong lensing information with weak lensing measurements over the whole cluster system ($600'' \times 600''$). The shapes of background galaxies necessary for weak lensing reconstruction were obtained from a comprehensive combination of our new *HST/ACS* imaging, the *VLT* data used in Cypriano et al. (2004), and from additional Subaru imaging. Our combined strong and weak lensing mass reconstruction (Fig. 3) resolves a complex structure, with at least four distinct peaks in the local mass distribution. The total mass of the cluster is $1.8 \pm 0.3 \times 10^{15} M_{\odot}$ within a radius of 1.3 Mpc, rendering Abell 2744, or *Pandora's Cluster*, similar in mass to the *Bullet Cluster*.

Chandra X-ray imaging also shows a complex arrangement of substructure. There are at least four X-ray ridges departing from the X-ray peak, including a Northern (NMRC) and a Southern (SMRC) ridge (Owers et al. 2011) . Interestingly, none of these coincide with any of the mass clumps found in our lensing mass reconstruction. Furthermore, the system also has a separate Northwestern X-ray feature with very low mass, also undetected in our lensing analysis. Observations of the gas temperature in this Northwestern feature (Kempner & David 2004; Owers et al. 2011) show a cold front pointing N-NE and a shock region ($T_X > 15$ keV) in the Southern ridge, for a projected impact velocity of 2150 km/s. That projected direction (SE-NW) therefore seems to define the primary merging event. However, in contrast to the proposed merging scenario of Owers et al. (2011) , we find the Southern ridge to be blueshifted with respect to the Northern ridge.

We also reveal that the Southern Core is ~ 2.5 times more massive than the Northern sub-clump – Owers et al. (2011) had expected this reversed – and that the secondary mass peak, which which it had the main collision, is in the Northwest. The mass ratio thus remains in agreement with general kinematical studies of Boschin et al. (2006), but swaps the sense of the collision from Owers et al. (2011). With this new scenario in hand, we repeated the velocity gradient analysis using the 'true' mass clumps (Core and Northwestern). These regions exhibit similar gas temperatures and metal abundances, and show evidence for a > 4900 km/s gradient with the Core region redshifted. These limits should be taken with caution, since the Chandra observations were not tailored specifically for velocity studies (they were obtained in different CCDs and at different epochs, so could be affected by variations in detector gain), and there is also some evidence of unknown calibration uncertainty between the two *ACIS-I* pointings taken of the same patch of sky. However, our results are consistent with the main merger having a significant component along the line-of-sight, with a magnitude and orientation consistent with that seen in the bi-modal distribution of galaxy velocities.

We also find evidence for a second merging event, simultaneously with or just before the main merger. The second merger, along the perpendicular NE-SW axis, was between today's Northern and Western mass peaks. We think these collided inside the extended halo of the core. During this dramatic collision, gas in today's Northern 'bullet' clump

was partially stripped by ram pressure, creating a characteristic separation between dark matter and baryons similar to that seen in the *Bullet Cluster*. The Western 'stripped' clump fared worse: all of its gas was removed, strewn into the tidal debris of the Core and a faint trail of excess X-ray emission towards its current location where we find just dark matter and galaxies.

The smaller merger may have enabled a curious effect in the main, SE-NW merger. We postulate that gas in the Core was puffed up by the first collision, reducing ram-pressure stripping during the second. We also suggest that the main merger could have included two separate subclumps incident along a filament from the SE. The combined effect would be an enhancement of the 'slingshot' effect proposed by Owers et al. (2011), by which the subclumps' gas was accelerated ahead of their dark matter. This would explain the very large $\sim 100''$ observed separation between any gas ('ghostly' clump or NW interloper), galaxies and dark matter ('dark' clump), as well as the double-peaked morphology of the dark clump. However, this scenario needs further confirmation.

The interpretation for this spectacular merging system will benefit immensely from additional observations and also from numerical simulations that can try to reproduce the new phenomenology shown in this cluster. The Western and Northwestern clumps have not been covered by *HST* observations and *Chandra* observations of the Western clump are shallow. Wide-field Subaru imaging in good seeing conditions and in several colours would also be useful to interpret the global environment. Numerical simulations should be performed to confirm the enhancement of the baryonic slingshot by the complicated merger configuration. The example of the *Bullet Cluster* has shown that the combination of complete lensing and X-ray observations (Markevitch et al. 2004; Bradač et al. 2006) with highly resolved hydrodynamical simulations (Springel & Farrar 2007; Randall et al. 2008) is a particularly powerful tool to understand the physics of merging clusters. In future work, we shall attempt to repeat this analysis on Abell 2744. The challenge laid down will be to explain the complicated phenomenology associated with this multiple merger, as well as to better constrain the collisional cross-section of dark matter, which our rough calculation suggests must be $\sigma/m = 3\ \mathrm{cm}^2\ \mathrm{g}^{-1}$, a tighter constraint than that from a similar analysis of the *Bullet Cluster*.

ADDITIONAL AFFILIATIONS

[9]Instituto de Astronomia, Geofísica e Ciências Atmosfericos, Universidade de São Paulo (IAG/USP), 05508-090 São Paulo/S.P.,Brazil
[10]Astronomical Institute, Tohoku University, Aramaki, Aoba-ku, Sendai 980-8578, Japan
[11]Academia Sinica Institute of Astronomy and Astrophysics (ASIAA), P.O. Box 23-141, Taipei 10617, Taiwan
[12]Department of Physics and Astronomy, 2130 Fulton St., University of San Francisco, San Francisco, CA 94117, USA
[13]Department of Physics and Astronomy, University of British Columbia, 6224 Agricultural Road, Vancouver, BC V6T 1Z1, Canada
[14]Instituto de Astrofísica de Andalucía (CSIC), C/Camino Bajo de Huétor 24, Granada 18008, Spain
[15]Department of Theoretical Physics, University of Basque Country UPV/EHU, Leioa, Spain
[16]IKERBASQUE, Basque Foundation for Science, 48011 Bilbao, Spain
[17]Jet Propulsion Laboratory, California Institute of Technology, 4800 Oak Grove Dr, MS 169-327, Pasadena, CA 91109, USA
[18]Spitzer Science Center, MS 220-6, California Institute of Technology, Jet Propulsion Laboratory, Pasadena, CA 91125, USA
[19]Department of Astronomy and Astrophysics, UCO/Lick Observatory, University of California, 1156 High Street, Santa Cruz, CA 95064, USA

ACKNOWLEDGEMENTS

The authors thank Matt Owers and Matthias Bartelmann for useful discussions. JM acknowledges financial support from the Heidelberg Graduate School of Fundamental Physics (HGSFP), the Agenzia Spaziale Italiana (ASI) and the Landesstiftung Baden-Württemberg. All runtime-expensive calculations were performed on dedicated GPU-machines at the Osservatorio Astronomico di Bologna. DC and RD acknowledge partial financial support from grant HST-GO-11689.09-A. RD also acknowledges support from NASA Grant NNH10CD19C. RM is supported by STFC Advanced Fellowship #PP/E006450/1 and ERC grant MIRG-CT-208994.

REFERENCES

Allen S. W., 1998, MNRAS, 296, 392
Anders E., Grevesse N., 1989, Geochim. Cosmochim. Acta, 53, 197
Andersson K. E., Madejski G. M., 2004, ApJ, 607, 190
Arnaud K. A., 1996, 101, 17
Ascasibar Y., Markevitch M., 2006, ApJ, 650, 102
Bartelmann M., Schneider P., 2001, Phys. Rep., 340, 291
Benítez N., 2000, ApJ, 536, 571
Bialek J. J., Evrard A. E., Mohr J. J., 2002, ApJ, 578, L9
Bond J. R., Cole S., Efstathiou G., Kaiser N., 1991, ApJ, 379, 440
Boschin W., Girardi M., Spolaor M., Barrena R., 2006, A&A, 449, 461
Bradač M., Allen S. W., Treu T., Ebeling H., Massey R., Morris R. G., von der Linden A., Applegate D., 2008, ApJ, 687, 959
Bradač M., Clowe D., Gonzalez A. H., Marshall P., Forman W., Jones C., Markevitch M., Randall S., Schrabback T., Zaritsky D., 2006, ApJ, 652, 937
Bradač M., Schneider P., Lombardi M., Erben T., 2005, A&A, 437, 39
Bradač M., Treu T., Applegate D., Gonzalez A. H., Clowe D., Forman W., Jones C., Marshall P., Schneider P., Zaritsky D., 2009, ApJ, 706, 1201
Braglia F., Pierini D., Böhringer H., 2007, A&A, 470, 425
Braglia F. G., Pierini D., Biviano A., Böhringer H., 2009, A&A, 500, 947
Bridle S. L., Kneib J., Bardeau S., Gull S. F., 2002, pp 38–46

Broadhurst T., Benítez N., Coe D., Sharon K., Zekser K., White R., Ford H., Bouwens R., Blakeslee J., 2005, ApJ, 621, 53
Carrasco E. R., Gomez P. L., Verdugo T., Lee H., Diaz R., Bergmann M., Turner J. E. H., Miller B. W., West M. J., 2010, ApJ, 715, L160
Clowe D., Bradač M., Gonzalez A. H., Markevitch M., Randall S. W., Jones C., Zaritsky D., 2006, ApJ, 648, L109
Clowe D., Gonzalez A., Markevitch M., 2004, ApJ, 604, 596
Coe D., Benítez N., Sánchez S. F., Jee M., Bouwens R., Ford H., 2006, AJ, 132, 926
Couch W. J., Newell E. B., 1984, ApJS, 56, 143
Cypriano E. S., Sodré Jr. L., Kneib J., Campusano L. E., 2004, ApJ, 613, 95
Czoske O., Moore B., Kneib J., Soucail G., 2002, A&A, 386, 31
Díaz-Giménez E., Zandivarez A., Proctor R., Mendes de Oliveira C., Abramo L. R., 2011, A&A, 527, A129+
Dickey J. M., Lockman F. J., 1990, ARA&A, 28, 215
Dupke R. A., Bregman J. N., 2001a, ApJ, 562, 266
Dupke R. A., Bregman J. N., 2001b, ApJ, 547, 705
Dupke R. A., Bregman J. N., 2006, ApJ, 639, 781
Dupke R. A., Mirabal N., Bregman J. N., Evrard A. E., 2007, ApJ, 668, 781
Erben T., Van Waerbeke L., Bertin E., Mellier Y., Schneider P., 2001, A&A, 366, 717
Evrard A. E., Metzler C. A., Navarro J. F., 1996, ApJ, 469, 494
Feng J. L., Kaplinghat M., Yu H., 2010, Physical Review Letters, 104, 151301
Finoguenov A., Sarazin C. L., Nakazawa K., Wik D. R., Clarke T. E., 2010, ApJ, 715, 1143
Giacintucci S., Venturi T., Macario G., Dallacasa D., Brunetti G., Markevitch M., Cassano R., Bardelli S., Athreya R., 2008, A&A, 486, 347
Giovannini G., Tordi M., Feretti L., 1999, New A, 4, 141
Girardi M., Mezzetti M., 2001, ApJ, 548, 79
Govoni F., Enßlin T. A., Feretti L., Giovannini G., 2001, A&A, 369, 441
Govoni F., Feretti L., Giovannini G., Böhringer H., Reiprich T. H., Murgia M., 2001, A&A, 376, 803
Grant C., 2001, ACIS Memo 195, space.mit.edu/ACIS/ps_files/ps195.ps.gz
Hallman E. J., Markevitch M., 2004, ApJ, 610, L81
Hayashi E., White S. D. M., 2006, MNRAS, 370, L38
Hoekstra H., 2007, MNRAS, 379, 317
Inogamov N. A., Sunyaev R. A., 2003, Astronomy Letters, 29, 791
Jee M. J., Blakeslee J. P., Sirianni M., Martel A. R., White R. L., Ford H. C., 2007, PASP, 119, 1403
Jee M. J., Ford H. C., Illingworth G. D., White R. L., Broadhurst T. J., Coe D. A., Meurer G. R., van der Wel A., Benítez N., Blakeslee J. P., Bouwens R. J., Bradley L. D., Demarco R., Homeier N. L., Martel A. R., Mei S., 2007, ApJ, 661, 728
Kaiser N., Squires G., Broadhurst T., 1995, ApJ, 449, 460
Kempner J. C., David L. P., 2004, MNRAS, 349, 385
Khosroshahi H. G., Ponman T. J., Jones L. R., 2007, MNRAS, 377, 595
Koekemoer A. M., Fruchter A. S., Hook R. N., Hack W., 2002, pp 337–+
Krist J., 2003, pp 6–+
Lacey C., Cole S., 1993, MNRAS, 262, 627
Leauthaud A., Massey R., Kneib J., Rhodes J., Johnston D. E., Capak P., Heymans C., Ellis R. S., Koekemoer A. M., 2007, ApJS, 172, 219
Lee J., Komatsu E., 2010, ArXiv e-prints, 1003.0939
Mahdavi A., Hoekstra H., Babul A., Balam D. D., Capak P. L., 2007, ApJ, 668, 806
Markevitch M., Gonzalez A. H., Clowe D., Vikhlinin A., Forman W., Jones C., Murray S., Tucker W., 2004, ApJ, 606, 819
Markevitch M., Gonzalez A. H., David L., Vikhlinin A., Murray S., Forman W., Jones C., Tucker W., 2002, ApJ, 567, L27
Markevitch M., Vikhlinin A., 2007, Phys. Rep., 443, 1
Massey R., 2010, MNRAS, 409, L109
Massey R., Rhodes J., Leauthaud A., Capak P., Ellis R., Koekemoer A., Réfrégier A., Scoville N., 2007, ApJS, 172, 239
Massey R., Stoughton C., Leauthaud A., Rhodes J., Koekemoer A., Ellis R., Shaghoulian E., 2010, MNRAS, 401, 371
Mastropietro C., Burkert A., 2008, MNRAS, 389, 967
Mathis H., Lavaux G., Diego J. M., Silk J., 2005, MNRAS, 357, 801
Meneghetti M., Rasia E., Merten J., Bellagamba F., Ettori S., Mazzotta P., Dolag K., Marri S., 2010, A&A, 514, A93+
Merten J., Cacciato M., Meneghetti M., Mignone C., Bartelmann M., 2009, A&A, 500, 681
Million E. T., Allen S. W., 2009, MNRAS, 399, 1307
Milosavljević M., Koda J., Nagai D., Nakar E., Shapiro P. R., 2007, ApJ, 661, L131
Miralda-Escudé J., 2002, ApJ, 564, 60
Morrison R., McCammon D., 1983, ApJ, 270, 119
Okabe N., Okura Y., Futamase T., 2010, ApJ, 713, 291
Okabe N., Takada M., Umetsu K., Futamase T., Smith G. P., 2010, PASJ, 62, 811
Okabe N., Umetsu K., 2008, PASJ, 60, 345
Owers M. S., Randall S. W., Nulsen P. E. J., Couch W. J., David L. P., Kempner J. C., 2011, ApJ, 728, 27
Pavlovsky C. e. a., 2006, Technical report, Advanced Camera for SurveysInstrument Handbook, version 7.1. Baltimore: STScI
Pawl A., Evrard A. E., Dupke R. A., 2005, ApJ, 631, 773
Randall S. W., Markevitch M., Clowe D., Gonzalez A. H., Bradač M., 2008, ApJ, 679, 1173
Rhodes J., Refregier A., Groth E. J., 2000, ApJ, 536, 79
Rhodes J. D., Massey R. J., Albert J., Collins N., Ellis R. S., Heymans C., Gardner J. P., Kneib J., Koekemoer A., Leauthaud A., Mellier Y., Refregier A., Taylor J. E., Van Waerbeke L., 2007, ApJS, 172, 203
Russell H. R., Sanders J. S., Fabian A. C., Baum S. A., Donahue M., Edge A. C., McNamara B. R., O'Dea C. P., 2010, MNRAS, 406, 1721
Sanders J. S., Fabian A. C., Smith R. K., 2011, MNRAS, 410, 1797
Sanders J. S., Fabian A. C., Smith R. K., Peterson J. R., 2010, MNRAS, 402, L11
Sarazin C. L., 2004, Journal of Korean Astronomical Society, 37, 433
Shan H., Qin B., Fort B., Tao C., Wu X., Zhao H., 2010, MNRAS, 406, 1134

Smail I., Ellis R. S., Dressler A., Couch W. J., Oemler Jr. A., Sharples R. M., Butcher H., 1997, ApJ, 479, 70
Smith R. K., Brickhouse N. S., Liedahl D. A., Raymond J. C., 2001, ApJ, 556, L91
Springel V., Farrar G. R., 2007, MNRAS, 380, 911
Sunyaev R. A., Norman M. L., Bryan G. L., 2003, Astronomy Letters, 29, 783
Tucker W., Blanco P., Rappoport S., David L., Fabricant D., Falco E. E., Forman W., Dressler A., Ramella M., 1998, ApJ, 496, L5+
Umetsu K., Medezinski E., Broadhurst T., Zitrin A., Okabe N., Hsieh B., Molnar S. M., 2010, ApJ, 714, 1470
Vikhlinin A., Kravtsov A. V., Burenin R. A., Ebeling H., Forman W. R., Hornstrup A., Jones C., Murray S. S., Nagai D., Quintana H., Voevodkin A., 2009, ApJ, 692, 1060
Williams L. L. R., Saha P., 2011, ArXiv e-prints
Zhang Y., Finoguenov A., Böhringer H., Ikebe Y., Matsushita K., Schuecker P., 2004, A&A, 413, 49
Zitrin A., Broadhurst T., Barkana R., Rephaeli Y., Benitez N., 2010, ArXiv e-prints, 1002.0521
Zitrin A., Broadhurst T., Coe D., Liesenborgs J., Benitez N., Rephaeli Y., Ford H., Umetsu K., 2010, ArXiv e-prints
Zitrin A., Broadhurst T., Umetsu K., Coe D., Benítez N., Ascaso B., Bradley L., Ford H., Jee J., Medezinski E., Rephaeli Y., Zheng W., 2009, MNRAS, 396, 1985
Zitrin A., Broadhurst T., Umetsu K., Rephaeli Y., Medezinski E., Bradley L., Jiménez-Teja Y., Benítez N., Ford H., Liesenborgs J., de Rijcke S., Dejonghe H., Bekaert P., 2010, MNRAS, 408, 1916
Zu Hone J. A., Lamb D. Q., Ricker P. M., 2009, ApJ, 696, 694
Zu Hone J. A., Ricker P. M., Lamb D. Q., Karen Yang H., 2009, ApJ, 699, 1004